

Spin polarization gate device based on the chirality-induced spin selectivity and robust nonlocal spin polarization

Hiroaki Shishido,^{1, a)} Yuta Hosaka,² Kenta Monden,² Akito Inui,² Taisei Sayo,² Yusuke Kousaka,¹ and Yoshihiko Togawa^{1, 3, b)}

¹⁾ *Department of Physics and Electronics, Osaka Metropolitan University, Sakai, Osaka 599-8531, Japan*

²⁾ *Department of Physics and Electronics, Osaka Prefecture University, Sakai, Osaka 599-8531, Japan*

³⁾ *Quantum Research Center for Chirality, Institute for Molecular Science, Okazaki 444-8585, Japan*

Nonlocal spin polarization phenomena are thoroughly investigated in the devices made of chiral metallic single crystals of CrNb_3S_6 and NbSi_2 as well as of polycrystalline NbSi_2 . We demonstrate that simultaneous injection of charge currents in the opposite ends of the device with the nonlocal setup induces the switching behavior of spin polarization in a controllable manner. Such a nonlocal spin polarization appears regardless of the difference in the materials and device dimensions, implying that the current injection in the nonlocal configuration splits spin-dependent chemical potentials throughout the chiral crystal even though the current is injected into only a part of the crystal. We show that the proposed model of the spin dependent chemical potentials explains the experimental data successfully. The nonlocal double-injection device may offer significant potential to control the spin polarization to large areas because of the nature of long-range nonlocal spin polarization in chiral materials.

I. INTRODUCTION

Conventional semiconductor devices based on electronics are well-established and widely used in modern society. For further development, in the last two decades, spin-based technologies, known as spin electronics, have attracted extensive attention as devices with new principles^{1,2}. In spin electronics devices, charge-to-spin current conversion is a crucial technology. Charge-to-spin current conversion is achieved by utilizing the spin Hall effect³⁻⁵, which was demonstrated initially in paramagnetic metals⁶ and now available even in topologically protected surface spin currents in topological insulators⁷⁻¹².

Chirality-induced spin selectivity (CISS) is another potential method for the charge-to-spin current conversion, where electrons flowing through a chiral material are spin-polarized reflecting the handedness of the material. The CISS phenomena were initially reported in chiral molecules via spin-polarized photocurrent emission¹³ and tunneling transport experiments¹⁴. Recent studies have shown that the spin polarization can be induced by the charge current due to the CISS effect in inorganic metals, such as in a paramagnetic state of chiral helimagnet CrNb_3S_6 ^{15,16}. It was observed that the spin polarization is dependent on the handedness of the crystals and is protected without charge current over $1\ \mu\text{m}$ in a nonlocal measurement configuration¹⁵. This record of the spin polarization length was updated to $10\ \mu\text{m}$ by measuring the CISS effect in nonmagnetic chiral crystals NbSi_2 and

TaSi_2 ¹⁷. Moreover, the CISS effect has been confirmed in polycrystalline samples of NbSi_2 and TaSi_2 . The spin polarization was observed even a few millimeters away from the charge current injection site¹⁸. The record of the spin polarization length is summarized in the literature¹⁹. Furthermore, it has been reported that the CISS effect is observed in single crystalline NbSi_2 samples of more than 6 cm in length²⁰.

In this paper, we demonstrate the spin polarization response induced by simultaneous nonlocal injection of charge currents from both sides of the crystal in micrometer-sized single and millimeter-sized polycrystalline chiral crystals. The superposition of spin polarization can be explained by the model that the current injection with the nonlocal setup induces the splitting of spin-dependent chemical potentials throughout the chiral crystal even when the current is injected into only a part of the sample. The controllability of spin polarization to large areas is successfully achieved in the nonlocal double-injection device made of chiral material.

II. EXPERIMENTAL METHODS

The hexagonal monoaxial chiral crystals of CrNb_3S_6 and NbSi_2 belong to the space group $P6_322$ (No. 182) and $P6_222$ (No. 180) or $P6_422$ (No. 181), respectively. In CrNb_3S_6 , Cr ions are intercalated between NbSi_2 layers resulting in a left- or right-handed crystal structure with lattice constants of $a = 0.57\ \text{nm}$ and $c = 1.21\ \text{nm}$, as illustrated in Fig. 1(a). NbSi_2 exhibits a C40-type crystal structure with lattice constants of $a = 0.4798\ \text{nm}$ and $c = 0.6592\ \text{nm}$, as shown in Fig. 1(b). CrNb_3S_6 shows monoaxial chiral helimagnetism below $132\ \text{K}$ ²¹⁻²³, whereas NbSi_2 exhibits diamagnetism and no magnetic order²⁴.

^{a)} Authors to whom correspondence should be addressed: H. Shishido, shishido@omu.ac.jp.

^{b)} Authors to whom correspondence should be addressed: Y. Togawa, ytogawa@omu.ac.jp.

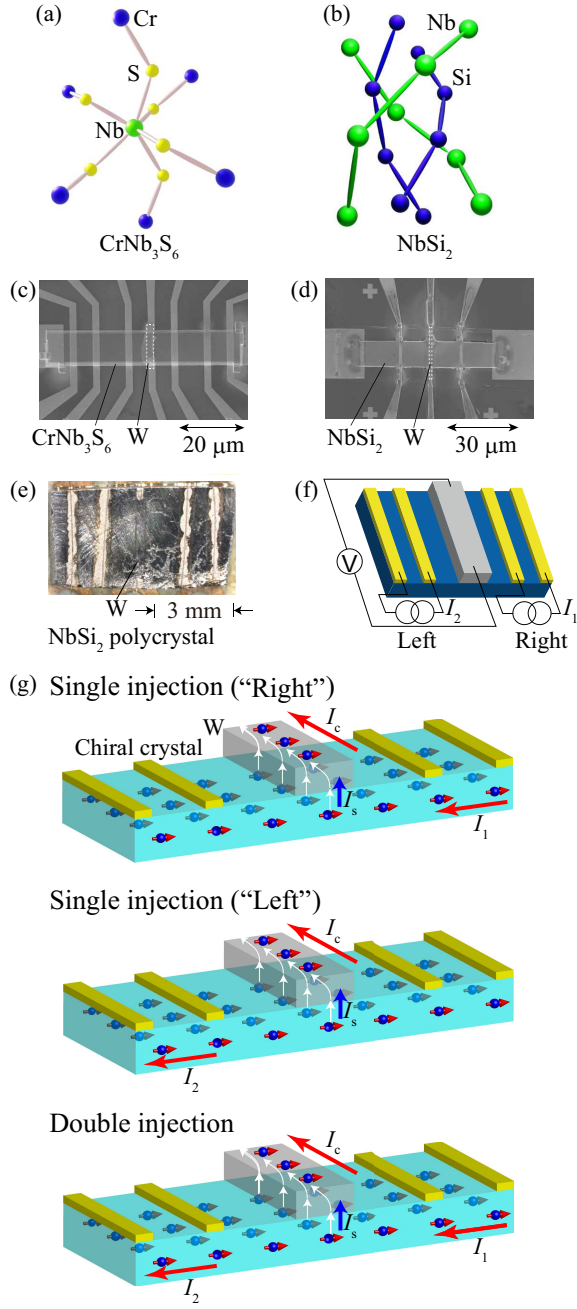


FIG. 1. Crystal structures of CrNb_3S_6 (a) and NbSi_2 (b). SEM images of the devices fabricated from single crystals of CrNb_3S_6 (c) and NbSi_2 (d). (e) The optical photograph of a device fabricated from NbSi_2 polycrystalline samples. (f) A schematic of the device structure and measurement configuration. The mechanism of device operation is schematically drawn in (g).

Single crystals of CrNb_3S_6 and NbSi_2 were grown using chemical vapor transport²⁵ and laser floating zone method²⁰, respectively. For the CISS measurements, samples were fabricated by using focused ion beam milling with dimensions of $60.8\ \mu\text{m}$ ($49.1\ \mu\text{m}$) in length, $11.2\ \mu\text{m}$ ($10.5\ \mu\text{m}$) in width, and $1.0\ \mu\text{m}$ ($1.0\ \mu\text{m}$) in

thickness for CrNb_3S_6 (NbSi_2), as shown in Fig. 1(c) [Fig. 1(d)]. Polycrystalline ingots of NbSi_2 were arc-melted in an Ar atmosphere from compound powders. Samples were cut from the bulk ingots with typical dimensions of several millimeters in length and width and of 1 mm in depth, as shown in Fig. 1(e).

In the present study, all the CISS measurements were performed at room temperature without applying any magnetic fields, ensuring that the contribution of the conventional Hall effect was excluded. Figure 1(f) shows the schematic of the device structure and CISS measurements. Four gold electrodes and a tungsten (W) electrode with a thickness of 6 nm are deposited on the chiral crystals. Charge currents I_1 and I_2 are applied into the “right” and “left” regions, respectively, which induce the spin polarization due to the CISS response, as schematically drawn in Fig. 1(g). The spin current I_s flows into the W electrode due to the difference in spin-dependent chemical potential between the chiral sample and the W electrode. The spin current in the W electrode is then converted to a transverse electrical current I_c via the inverse spin Hall effect (SHE)^{6,26,27}. Note that NbSi_2 is a diamagnetic metal and thus has no localized spins. CrNb_3S_6 is in a paramagnetic state at room temperature. Therefore, the present transverse voltage is not induced by the anomalous Hall effect (AHE) but by the inverse SHE via the CISS. This is in contrast with the previous study using chiral metallo-bio-organic crystals, where a transverse voltage is induced by the AHE due to the ferromagnetic property of the crystals²⁸.

III. EXPERIMENTAL RESULTS AND DISCUSSION

A. Nonlocal CISS signals with conventional setup (for single injection of charge current)

Figure 2 displays the CISS signal V as a function of the applied current I using the nonlocal setup. The linear I - V characteristics of the nonlocal CISS signals were observed not only in the micrometer-sized single crystals of CrNb_3S_6 [Fig. 2(a)] and NbSi_2 [Fig. 2(b)] but also in the bulk polycrystalline NbSi_2 [Fig. 2(c)], as previously reported in other publications^{15,17,18}.

Notably, the distance between current and voltage contacts of bulk polycrystalline samples is 1.5 mm, which is two order of magnitude longer than those of micrometer-sized single crystals. The V/I slope is $0.3\ \Omega$ in the single crystal CrNb_3S_6 , while it is about $3\ \text{m}\Omega$ and $0.1\ \text{m}\Omega$ in the single and polycrystal NbSi_2 , respectively. These slope intensities are of the same order as those reported in previous studies^{15,17,18}, suggesting a successful observation of the CISS phenomena.

The sign of the slope is determined by the handedness at the current injected region of chiral crystals^{15,17}. Observing the same signs in the “left” and “right” sides for the CrNb_3S_6 and polycrystalline NbSi_2 indicates the

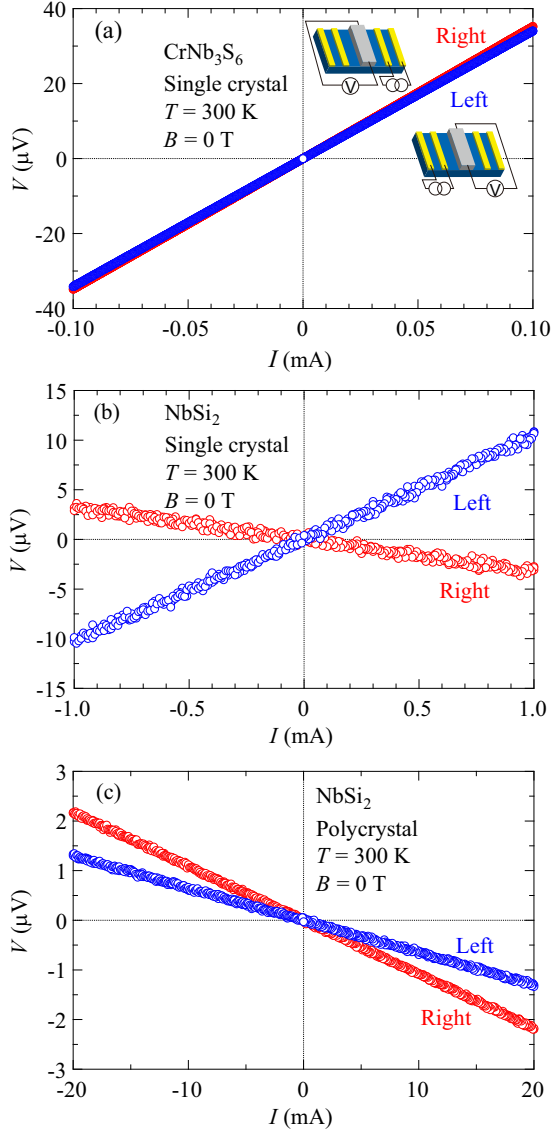


FIG. 2. The nonlocal CISS signals for (a) CrNb_3S_6 single crystals, (b) NbSi_2 single crystals, and (c) bulk polycrystalline NbSi_2 . All the measurements were performed at room temperature without magnetic fields.

same handedness in both regions. In contrast, the opposite signs observed in the single crystalline NbSi_2 denote the opposite handedness in the “left” and “right” regions.

B. Nonlocal CISS signals for double injection of charge currents with nonlocal setup

When charge currents are simultaneously injected into the “left” and “right” regions, the CISS signal appears as a superposition of the CISS signals, separately induced by the current injection into each regions. Figure 3 shows that the linearity of the I - V curves with regard to the current (I_1) injected into the “right” region is maintained

even when the additional current (I_2) is injected into the “left” region. In addition, the I - V curves shift upward or downward as a function of I_2 injected into the “left” region. The polarity and intensity of the shifts are consistent with those expected from the I - V curves for the single injection of charge current, shown in Fig. 2.

On the basis of the I - V characteristics for the double injection of charge currents with the nonlocal setup, we demonstrate that the CISS output is controllable in terms of the polarity and intensity of the signal. Figure 4 indeed shows such switching behavior of the CISS signal against the input charge currents I_1 and I_2 .

For the single injection of input current into the single crystal of CrNb_3S_6 [see the first five columns in Fig. 4(a)], the CISS signal becomes 33.8 and $-33.5 \mu\text{V}$ for $I_1 = 0.96$ and -0.96 mA, respectively, with I_2 being 0 mA. Alternatively, the input current of $I_2 = 1.00$ and -1.00 mA

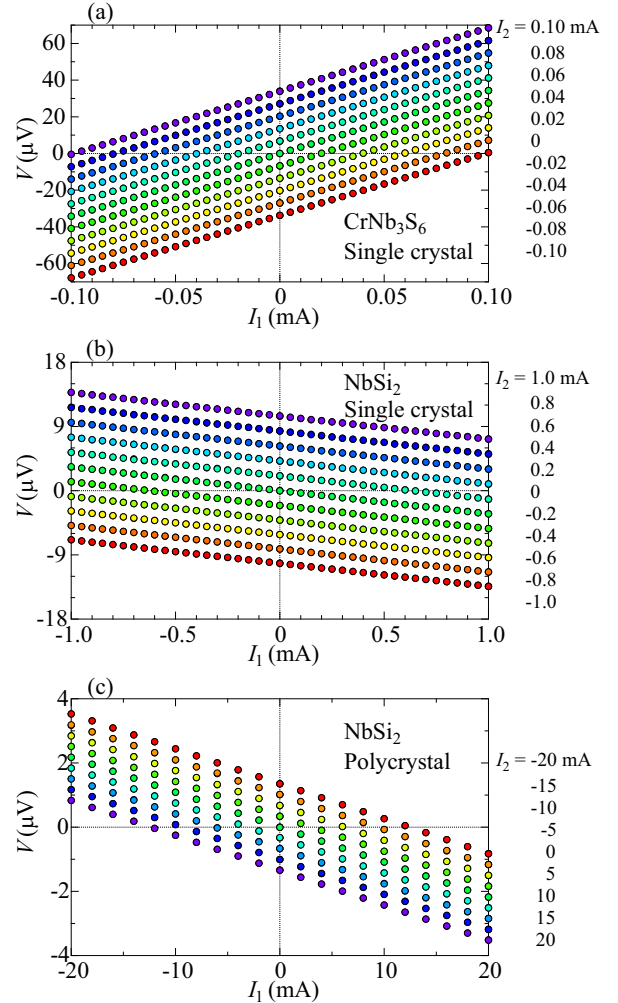


FIG. 3. A dataset of I - V characteristics is provided for the charge current (I_1) injected into the “right” region for (a) single crystals of CrNb_3S_6 , (b) single crystals of NbSi_2 , and (c) polycrystalline NbSi_2 , under various injection charge currents I_2 into the “left” region.

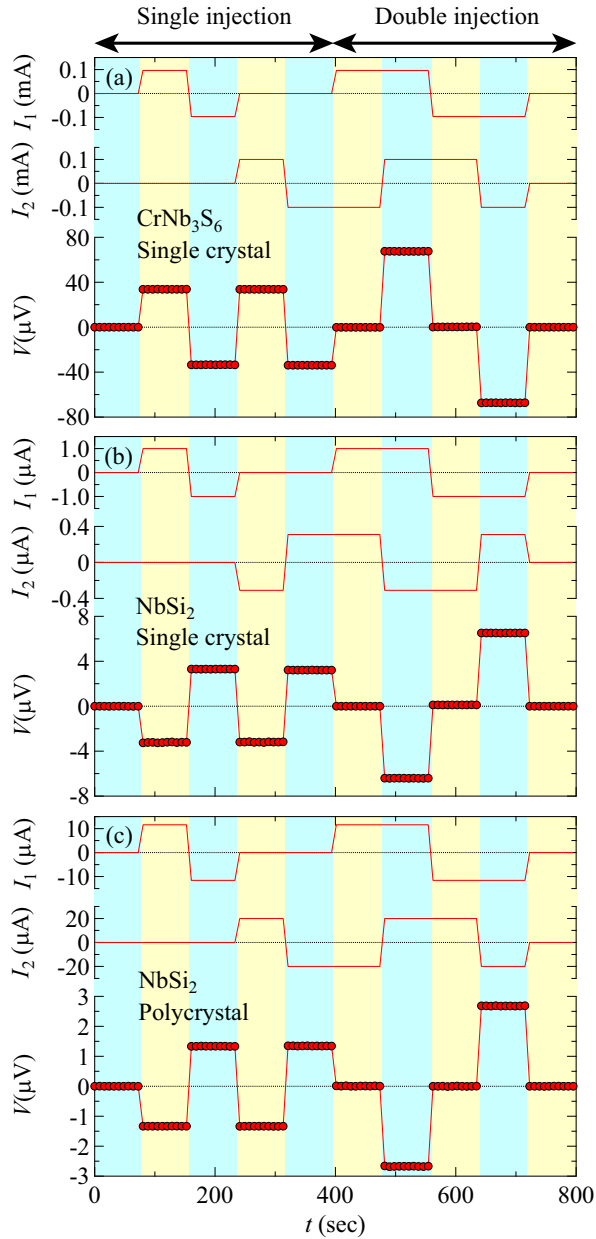


FIG. 4. Dependence of the CISS signals on the double injection of charge currents with the nonlocal setup for CrNb_3S_6 single crystals (a), NbSi_2 single crystals (b), and polycrystalline NbSi_2 (c). The input charge currents were injected into the “right” (I_1) and “left” (I_2) regions. First five columns in the panels represent the single injection of input current, while the latter five columns correspond to the operation of double injection.

with I_1 fixed to be 0 mA results in the CISS signal of 33.7 and $-33.8 \mu\text{V}$, respectively, the intensities of which are almost as large as the those obtained for the former case (by the I_1 injection).

Next, let us see the operation of double injection, as shown in the latter five columns in Fig. 4(a). The CISS signal is suppressed to be less than $0.3 \mu\text{V}$ for the simul-

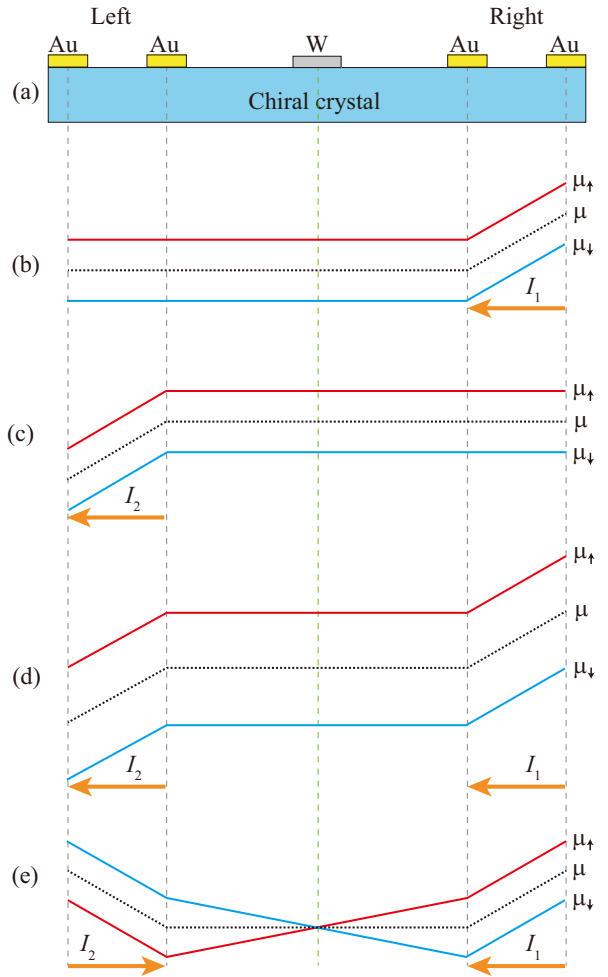


FIG. 5. Schematics of the spin-dependent chemical potentials induced by the double injection of charge currents in the nonlocal configuration. (a) Side view of a CISS device for the double injection. The distribution of spin-dependent chemical potentials triggered by the single injection of charge current on the “right” (b) and “left” regions (c). The double injection of charge currents flowing in the same direction gives the same polarity of the CISS signals and, thus, enhances the potential difference at the center region, as shown in (d). On the other hand, the charge currents with the opposite direction in the nonlocal setup induce the opposite polarity of the CISS signals and, thus, the potential difference intersects at the center, as shown in (e).

taneous injection of input currents $(I_1, I_2) = (0.96, -1.00)$ or $(-0.96, 1.00)$, given in the unit of mA. On the other hand, the CISS signal reaches 67.5 and $-67.3 \mu\text{V}$ for the double injection of $(I_1, I_2) = (0.96, 1.00)$ and $(-0.96, -1.00)$, respectively.

Similar switching behavior of the CISS signals is also obtained for the double injection of charge currents with the nonlocal setup in single crystals and bulk polycrystals of NbSi_2 , as shown in Figs. 4(b) and 4(c).

We deduce the spin-dependent chemical potentials across the CISS device from the double-injection CISS re-

response. First, injecting the charge currents in the nonlocal configuration induces the CISS effect, which splits the spin-dependent chemical potentials. Importantly, such a split between the up-spin chemical potential μ_{\uparrow} and down-spin chemical potential μ_{\downarrow} should be transmitted over the chiral crystal without any additional local current, as shown in Figs. 5(b) and 5(c). This picture is supported by the long-range spin polarization observed in the nonlocal measurements. The direction of the split depends on the direction of the injected current and handedness of the crystal. Here, for simplicity, the device is assumed to be made of the enantio-pure crystal.

When the charge currents with the same polarity are injected into both sides of the crystal, as illustrated in Fig. 5(d), the splits between μ_{\uparrow} and μ_{\downarrow} are added over the crystal and thus the intensified CISS signal is detected at the center of the device, where the W electrode is deposited. Conversely, when the polarities of the injected charge currents are opposite to each other, μ_{\uparrow} and μ_{\downarrow} intersect at the center of the device, as shown in Fig. 5(e). Consequently, no CISS signal is detected since μ_{\uparrow} and μ_{\downarrow} degenerate at the center of the device. Note that the split between μ_{\uparrow} and μ_{\downarrow} may vary along the device, which could potentially induce the potential difference even at the center region and might generate the spin current into the W electrode. Interestingly, up-spin electrons flow leftward in the chiral material, while down-spin electrons flow rightward because of a spatial gradient of the chemical potential. In particular, a pure spin current flows even in the chiral material in this situation.

To confirm the validity of our spin-dependent chemical potentials model, a spatial distribution of the CISS signals was examined in a bulk NbSi₂ double-injection CISS device with the three W electrodes, as shown in Fig. 6. It is expected that, when the charge currents in the nonlocal configuration with the opposite polarity are applied, μ_{\uparrow} and μ_{\downarrow} degenerate at the center of the device, resulting in the disappearance of the CISS signal at the center (W2) electrode. However, the difference between μ_{\uparrow} and μ_{\downarrow} should remain finite and opposite in the right and left regions distant from the center. Therefore, finite CISS signals with the opposite polarity could be detected at the left (W1) and right (W3) electrodes, as shown in Fig. 6(c).

The CISS signals with the input currents (I_1, I_2) = (20, -5.8) and (-20, 5.8), in the unit of mA, are presented in Fig. 6(d). A finite CISS signal of -0.70 and $0.70 \mu\text{V}$ respectively appears at the W1 electrode, whereas that of 10.6 and $-10.6 \mu\text{V}$ is observed at the W3 electrode. In contrast, the CISS signals at the W2 electrode are less than 2 nV in both cases. Precisely speaking, in the experiments, the combination of I_1 and I_2 values was tuned to minimize the CISS signal at the W2 electrode. Then, the CISS signals at the W1 and W3 electrodes were monitored. The present observations are qualitatively consistent with our expectation based on the spin-dependent chemical potential model, which predicts finite CISS sig-

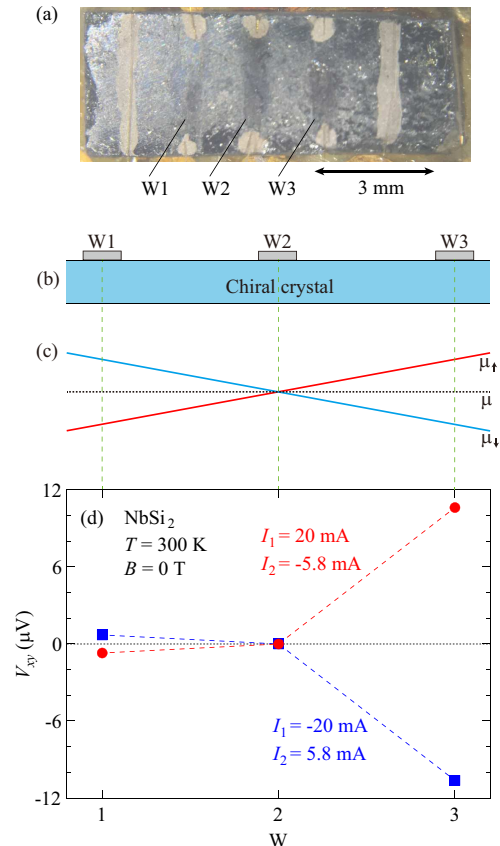


FIG. 6. (a) The optical photograph of the double-injection CISS device with the three W electrodes. (b) A schematic of the side-view of the device and (c) the distribution of spin-dependent chemical potentials along the chiral crystal. (d) The nonlocal CISS signals detected at each W electrode for the double injection of charge currents.

nals with the opposite polarity at the W1 and W3 electrodes and no CISS signal at the W2 electrode.

C. Absorption of spin polarization by W electrodes (for single injection of charge current)

The data in Fig. 6(d) shows the difference in the CISS intensity between the W1 and W3 electrodes, which may indicate some features beyond the naive picture given in Fig. 6(c). In particular, the presence of additional W electrodes may cause a reduction in the CISS signal.

To see the influence of the additional W electrodes, the nonlocal CISS signals were examined in the same device with the three W electrodes as that used in Fig. 6. Figure 7 shows that the signal intensity gradually decreases from the “left” region in the single injection of charge current. Conversely, when the current is injected into the “right” region, the signal intensity displays a steep increase from the left to the right. With an increase in the number of W

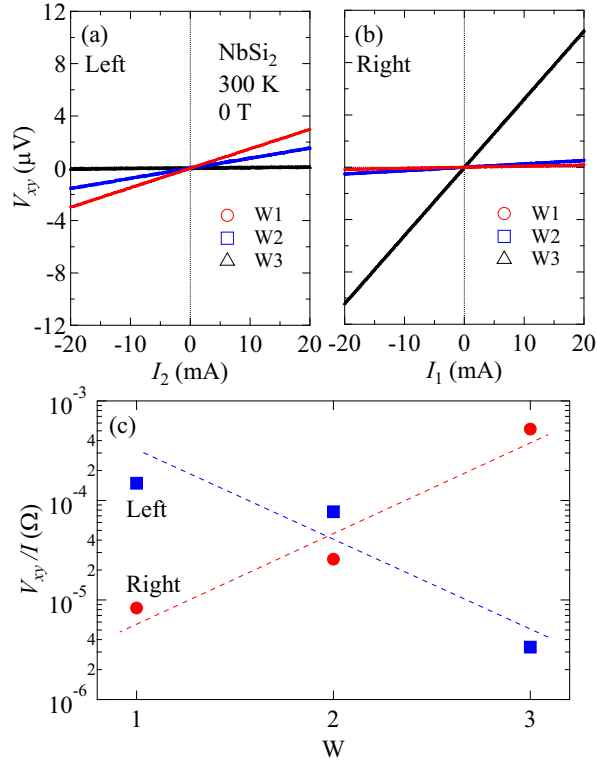


FIG. 7. The CISS signals at the three W electrodes with the single injection of charge current into “left” (a) and “right” (b) regions. The slope V_{xy}/I is summarized in (c), where the dashed lines are provided as a guide to the eyes.

electrodes in the direction away from the current injection region, the nonlocal CISS signal appears to decrease. Furthermore, this result indicates that the split of spin-dependent chemical potentials reduces by the absorption of the spin current into the W electrode.

IV. SUMMARY

The nonlocal CISS measurements were thoroughly performed in the double-injection CISS devices made of several chiral materials with different dimensions. The data shows qualitatively similar response of spin polarization, regardless of the difference in materials and device sizes. Furthermore, it is demonstrated that the CISS response could be identified by using the model of spin-dependent chemical potentials, which is derived from the long-range spin polarization in chiral materials. In addition, we argue the possibility that the spin polarization decreases each time when the spin current is absorbed into the W electrode.

The double-injection CISS device may offer significant potential to revolutionize the spin polarization response in the electronic devices. Importantly, these devices can work over a wide range of dimensions due to the nature of long-range spin polarization and operate on the basis

of spin polarization rather than electron (charge) flow or accumulation, which ensures a large reduction of heat generation caused by Joule heating. A wide range of chiral materials could be utilized for fabricating the spin polarization devices.

SUPPLEMENTARY MATERIAL

The supplementary material shows a temperature dependence of the CISS signals in the NbSi₂ polycrystalline device used in Figs. 6 and 7. A different temperature dependence was obtained in the transverse and longitudinal signals, indicating that the present transverse signal is not due to misalignments of the detection electrodes but to the intrinsic CISS effect.

ACKNOWLEDGMENTS

We sincerely thank Yusuke Kato and Hiroaki Kusunose for fruitful discussions. We acknowledge support from Grants-in-Aid for Scientific Research (Grant Nos. 17H02767, 17H02923, 21H01032, 22H01944, and 23H00091) and the Research Grant of Specially Promoted Research Program by Toyota RIKEN, and the Joint Research by Institute for Molecular Science (IMS program No. 23IMS1101).

DATA AVAILABILITY STATEMENT

The data supporting the findings of the present study is available from the corresponding authors upon request.

REFERENCES

- ¹G. A. Prinz, *Magnetoelectronics*, *Science* **282**, 1660-1663 (1998).
- ²S. A. Wolf, D. Awschalomr, A. Buhrmanj, M. Daughtons, S. V. Molnár, L. Roukesa, Y. Chtchelkanovaand, and D. M. Treger, *Spintronics: A spin-based electronics vision for the future*, *Science* **294**, 1488-1495 (2001).
- ³M. I. Dyakonov, and V. I. Perel, *Current-induced spin orientation of electrons in semiconductors*, *Phys. Lett.* **35**, 459-460 (1971).
- ⁴J. E. Hirsch, *Spin Hall effect*, *Phys. Rev. Lett.* **83**, 1834-1837 (1999).
- ⁵S. Zhang, *Spin Hall effect in the presence of spin diffusion*, *Phys. Rev. Lett.* **85**, 393-396 (2000).
- ⁶S. O. Valenzuela and M. Tinkham, *Direct electronic measurement of the spin Hall effect*, *Nature* **442**, 176 (2006).
- ⁷Y. Shiomi, K. Nomura, Y. Kajiwara, K. Eto, M. No-vak, Kouji Segawa, Yoichi Ando, and E. Saitoh, *Spin-*

- electricity conversion induced by spin injection into topological insulators, *Phys. Rev. Lett.* **113**, 196601 (2014).
- ⁸C. H. Li, O. M. J. van'tErve, J. T. Robinson, Y. Liu, L. Li, and B. T. Jonker, Electrical detection of charge-current-induced spin polarization due to spin-momentum locking in Bi_2Se_3 , *Nat. Nanotechnol.* **9**, 218-224 (2014).
- ⁹A. R. Mellnik, J. S. Lee, A. Richardella, J. L. Grab, P. J. Mintun, M. H. Fischer, A. Vaezi, A. Manchon, E.-A. Kim, N. Samarth, and D. C. Ralph, Spin-transfer torque generated by a topological insulator, *Nature* **511**, 449-451 (2014).
- ¹⁰Y. Fan, P. Upadhyaya, X. Kou, M. Lang, S. Takei, Z. Wang, J. Tang, L. He, L.-T. Chang, M. Montazeri, G. Yu, W. Jiang, T. Nie, R. N. Schwartz, Y. Tserkovnyak, and K. L. Wang, Magnetization switching through giant spin-orbit torque in a magnetically doped topological insulator heterostructure, *Nat. Mater.* **13**, 699-704 (2014).
- ¹¹Y. Ando, T. Hamasaki, T. Kurokawa, K. Ichiba, F. Yang, M. Novak, S. Sasaki, K. Segawa, Y. Ando, and M. Shiraishi, Electrical detection of the spin polarization due to charge flow in the surface state of the topological insulator $\text{Bi}_{1.5}\text{Sb}_{0.5}\text{Te}_{1.7}\text{Se}_{1.3}$, *Nano Lett.* **14**, 6226-6230 (2014).
- ¹²P. Deorani, J. Son, K. Banerjee, N. Koirala, M. Brahlek, S. Oh, and H. Yang, Observation of inverse spin Hall effect in bismuth selenide, *Phys. Rev. B* **90**, 094403 (2014).
- ¹³B. Göhler, V. Hamelbeck, T. Z. Markus, M. Kettner, G. F. Hanne, Z. Vager, R. Naaman, H. Zacharias, Spin selectivity in electron transmission through self-assembled monolayers of double-stranded DNA, *Science* **331**, 894 (2011).
- ¹⁴Z. Xie, T. Z. Markus, S. R. Cohen, Z. Vager, R. Gutierrez, R. Naaman, Spin specific electron conduction through DNA oligomers, *Nano Lett.* **11**, 4652 (2011).
- ¹⁵A. Inui, R. Aoki, Y. Nishiue, K. Shiota, Y. Kousaka, H. Shishido, D. Hirobe, M. Suda, J. Ohe, J. Kishine, H. Yamamoto, Y. Togawa, Chirality-induced spin-polarized state of a chiral crystal CrNb_3S_6 , *Phys. Rev. Lett.* **124**, 16602 (2020).
- ¹⁶Y. Nabei, D. Hirobe, Y. Shimamoto, K. Shiota, A. Inui, Y. Kousaka, Y. Togawa, and H. M. Yamamoto, Current-induced bulk magnetization of a chiral crystal CrNb_3S_6 , *Appl. Phys. Lett.* **117**, 052408 (2020).
- ¹⁷K. Shiota, A. Inui, Y. Hosaka, R. Amano, Y. Onuki, M. Hedo, T. Nakama, D. Hirobe, J. Ohe, J. Kishine, H. M. Yamamoto, H. Shishido, and Y. Togawa, Chirality-induced spin polarization over macroscopic distances in chiral disilicide crystals, *Phys. Rev. Lett.* **127**, 126602 (2021).
- ¹⁸H. Shishido, R. Sakai, Y. Hosaka, Y. Togawa Appl. Detection of chirality-induced spin polarization over millimeters in polycrystalline bulk samples of chiral disilicides NbSi_2 and TaSi_2 , *Phys. Lett.* **119**, 182403 (2021).
- ¹⁹Y. Togawa, A. S. Ovchinnikov, and J. Kishine, Generalized Dzyaloshinskii-Moriya interaction and chirality-induced phenomena in chiral crystals, *J. Phys. Soc. Jpn.* **92**, 081006 (2023).
- ²⁰Y. Kousaka, T. Sayo, S. Iwasaki, R. Saki, C. Shimada, H. Shishido, and Y. Togawa, Chirality-selected crystal growth and spin polarization over centimeters of transition metal disilicide crystals, *Jpn. J. Appl. Phys.* **62**, 015506 (2023).
- ²¹T. Miyadai, K. Kikuchi, H. Kondo, S. Sakka, M. Arai, and Y. Ishikawa, Magnetic properties of $\text{Cr}_{1/3}\text{NbS}_2$, *J. Phys. Soc. Jpn.* **52**, 1394 (1983).
- ²²Y. Togawa, T. Koyama, K. Takayanagi, S. Mori, Y. Kousaka, J. Akimitsu, S. Nishihara, K. Inoue, A. S. Ovchinnikov, and J. Kishine, Chiral magnetic soliton lattice on a chiral helimagnet, *Phys. Rev. Lett.* **108**, 107202 (2012).
- ²³Y. Togawa, Y. Kousaka, K. Inoue, and J. Kishine, Symmetry, structure, and dynamics of monoaxial chiral magnets, *J. Phys. Soc. Jpn.* **85**, 112001 (2016).
- ²⁴U. Gottlieb, A. Sulpice, R. Madar, and O. Laborde, Magnetic susceptibilities of VSi_2 , NbSi_2 and TaSi_2 single crystals, *J. Phys.: Condens. Matter* **5**, 8755 (1993).
- ²⁵Y. Kousaka, Y. Nakao, J. Kishine, M. Akita, K. Inoue, and J. Akimitsu, Chiral helimagnetism in $\text{T}_{1/3}\text{NbS}_2$ (T=Cr and Mn), *Nucl. Instrm. Methods Phys. Res., Sect. A* **600**, 250 (2009).
- ²⁶E. Saitoh, M. Ueda, H. Miyajima, G. Tatara, Conversion of spin current into charge current at room temperature: Inverse spin-Hall effect, *Appl. Phys. Lett.* **88**, 182509 (2006).
- ²⁷T. Kimura, Y. Otani, T. Sato, S. Takahashi, S. Maekawa, Room-temperature reversible spin Hall effect, *Phys. Rev. Lett.* **98**, 156601 (2007).
- ²⁸N. Goren, T. K. Das, N. Brown, S. Gilead, S. Yochelis, E. Gazit, R. Naaman, Y. Paltiel, Metal organic spin transistor, *Nano Lett.* **21**, 8657 (2021).

Supplemental Materials for
“Spin polarization gate device based on the chirality-induced spin selectivity and robust nonlocal spin polarization”

V. TEMPERATURE DEPENDENCE OF CISS SIGNALS

A temperature dependence of the longitudinal resistance R_{xx} and CISS signals V_{xy} was examined with the polycrystalline NbSi₂ with the three W electrodes, shown in Fig. 6(a). R_{xx} was measured with the standard four-probe method, in which the current was applied through the electrodes attached to the side of sample and the longitudinal voltage V_{xx} was detected between the inner electrodes. V_{xy} was measured at the three W electrodes in the “center” region, where R_{xx} was measured, as schematically shown in the inset of Fig. S1(a).

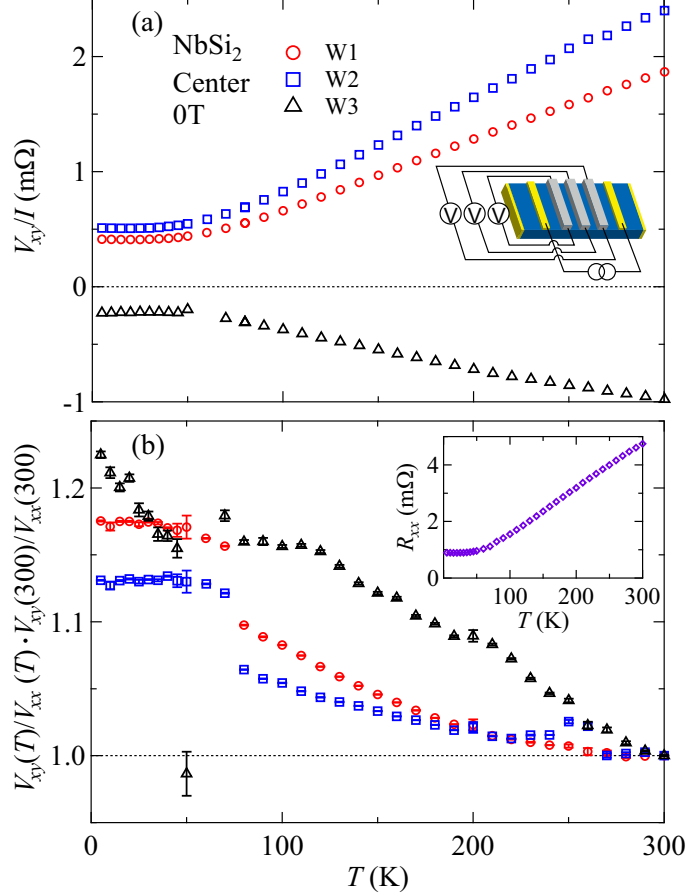


FIG. S1. Temperature dependence of (a) CISS signals V_{xy}/I in the “center” region, and (b) signal ratio of V_{xy} and V_{xx} normalized at 300 K for bulk polycrystalline NbSi₂ with the three W detection electrodes. The inset in (b) shows the temperature dependence of the longitudinal resistance R_{xx} .

V_{xy} observed at the W3 detection electrode exhibits the opposite polarity to those at the W1 and W2 electrodes even though the same electrodes are used for the charge current application.

These results exclude the contribution of nonuniform charge currents due to local resistance changes in the crystal and electrodes. Rather, the results suggest that the polarity of transverse signals reflects a distribution of the handedness under the detection electrodes and thus are due to the CISS effect.

V_{xy} decreases with reducing temperature and reaches the residual values, as shown in Fig. S1(a). R_{xx} , shown in the inset of Fig. S1(b), exhibits a typical temperature dependence of normal metals. The signal ratio of V_{xy}/V_{xx} , which is normalized at 300 K, is shown as a function of temperature in Fig. S1(b). The ratio increases with decreasing temperature, clarifying different temperature dependences of V_{xy} and V_{xx} . This observation indicates that the present transverse voltage is not due to misalignments of the detection electrodes but to the intrinsic CISS effect.